ORIGINAL RESEARCH

Demonstrating the Relationship Between the Colour and Heavy Element Abundance of Globular Clusters

Guillaume Hewitt[1]

1. McMaster University, Integrated Science, Class of 2022

SUMMARY

Globular clusters are dense collections of the oldest stars in the universe, ranging from 11 to 13 billion years old. The stars that make up the clusters share common characteristics, such as their heavy element abundance (metallicity), as they are formed at the same time from the same dust cloud. Globular clusters outside the Milky Way are only seen as a single point of light, not as individual stars. This study investigates how the metallicity of clusters affects the colour light they emit. Colour-metallicity diagrams were created from 11 theoretical cluster models. Results showed that there was a relationship between the amount of heavy element abundance and the colour of light emitted. This relationship was then placed on the clusters from the real galaxy NGC 6166. The distribution of metallicities this gave was not a simple normal curve. This suggests that NGC 6166 merged with other globular clusters at some point in time, which is consistent with the literature.

ABSTRACT

Extragalactic globular clusters are viewed as single points of light, as the density of their stars make them individually indiscernible. The aim of this study was to find a correlation between the integrated colour of globular star clusters and the metallicity of their individual stars. This was accomplished by using the colour magnitudes and metallicities of individual stars from 11 cluster models based on work from Girardi et al. Integrated colour-metallicity diagrams found the relationship between clusters   to be an increasing two-step linear function for each of the six colour ratios examined. To validate these findings, the F475W-F814W relationship was applied to integrated colour data of 5557 clusters from the real galaxy NGC 6166. Histograms taken of the colour and metallicity both showed non-gaussian distributions. Bimodal gaussian fits were applied to both and found that each exhibited the presence of subpopulations: one metal-poor ($\mu = -1.59$), and one metal-rich ($\mu = -0.41$). This suggests the occurrence of galactic mergers with NGC 6166 to create the population structure of clusters that is currently seen.

Keywords: Globular clusters, isochrones, colour-metallicity diagrams

INTRODUCTION

Globular clusters are collections of stars that are gravitationally bound in a distinct spherical shape (Figure 1). The clusters orbit a parent galaxy, residing in the surrounding galactic halo, displaying as much of a spherical symmetry as the galaxy itself does.[1] The vast number of stars they contain in their relatively small system, gives them some of the highest stellar densities in the galactic vicinity. The clusters around the Milky Way galaxy have an average of 200,000 $M_\odot$ (solar masses) and a tidal (boundary) radius of $\sim$ 50 pc, giving them a range of average densities from 0.2 $M_\odot$ pc^{-3} at their boundaries up to 10^4 $M_\odot$ pc^{-3} at their cores.[2] As of 2010, there have been 158 confirmed globular clusters around the Milky Way, with a hand-ful more possibly residing on the other side of the galactic disk, in which infrared imaging might be able to locate them.[3,4] The positioning of the clusters around the galactic core is what the astronomer Harlow Shapley used to dispel the notion that the solar system resided in the center of the galaxy.[5] In addition, the immense age of some clusters (reaching up to 13 billion years (Gyr)) allowed for a fundamental lower limit of the age of the universe to be set, as the universe must be older than the stars it holds.

Figure 1. Hubble image of NGC 7006, one of the globular clusters surrounding the Milky Way.[6]

There are two major sub-groups of globular clusters. The first contains the older metal-poor clusters, which emit more blue light, and approach an age of 13 Gyr. The second subgroup includes the younger metal-rich clusters, which emit more red light, and sit around 11 Gyr.[7] These ages can only be discerned for the populations that exist in the Milky Way and its surrounding satellites, for reasons that will soon be mentioned. Aging the clusters is achieved through isochrone fitting to their respective stellar sequences. An isochrone is a specific curve or track on the Hertzsprung-Russell (H-R) diagram that consists of stars with the same age (Figure 2). Stellar clusters (both globular and open) are well disposed for this, as the entire population is born out of the same homogenous cloud at relatively the same time.[8] The only varying factor between them is their mass, the stars. As a result, when they are plotted in terms of their luminosity and surface temperatures, it will yield a unique path that at some point deviates from the standard line of hydrogen burning stars, which is deemed the zero-age main sequence.[1]

The most common method of plotting globular cluster stars is on a colour-magnitude diagram, which is created with just the magnitudes of two distinct wavelength filters of each star in the cluster.[8] Pre-determined isochrones are fitted to the plot in the hopes of matching the position where the stars begin to deviate, called the main sequence turn-off point. This point, which leads to further evolutionary tracks such as the red giant branch and the horizontal branch, moves downwards towards the smaller, less luminous stars as time progresses, allowing for anticipatory dynamic motions in the tracks.[9] Figure 3 shows an example of how theoretical isochrones can be fitted

to a real population of stars (in this case using a H-R diagram), thereby giving further detail and structure of age and direction to an otherwise chaotic diagram.
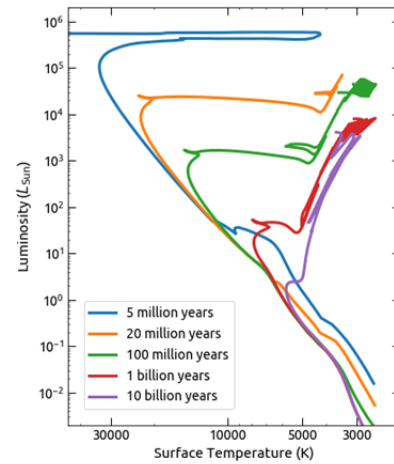

Figure 2. Theoretical isochrones from the stellar models by Leo Girardi and collaborators (Padova) for near-solar metallicity and a range of ages.[10]
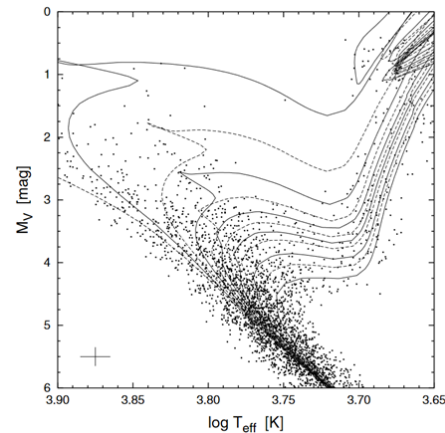

Figure 3. A Hertzsprung-Russell diagram of 2968 artificial stars overlayed with isochrones that span from 1 Gyr at the top to 15 Gyr at the bottom.[11]

Globular clusters can be found around any galaxy in the Local Group (which includes the Milky Way, Andromeda, and their respective satellite galaxies) with sufficient mass. The amount of clusters orbiting is also proportional to the dynamical mass of the host galaxy.[12] However, when looking at increasingly distant extra-galactic clusters, the ability to discern their individual stars becomes more and more difficult. Eventually, the light that is collected comes as a singular entity, in which any information that is extracted will be measuring the integrated properties of that cluster.[8] Without the individual star data, colour-magnitude diagrams are ineffective, and isochrone fitting cannot be done. Therefore, we must look to more immediate clusters to extrapolate the trends they would hold if viewed as a single, composite object.

METHODS

The initial work was begun using 11 cluster models computed from Girardi's *CMD* web interface. Each were created using a compilation of research on stellar populations and their tracks.[13–18] The models were created on October 15, 2019, using the *CMD 3.3* configuration. The data extracted from each model and used for this project included the cluster metallicity, the log of the luminosity of each star, the log of the effective temperature of each star, as well as the magnitudes of each star in the light filters of *F435W*, *F475W*, *F555W*, *F606W*, *F814W*, and *F850LP*. Table 1 includes additional information on the scale and metallicity of each cluster.

Table 1. The number of stars and the metallicity of each of the 11 clusters used for the analysis.

Cluster	Number of Stars	Metallicity (Z)
Girardi +0.2	137131	0.02259
Girardi 0.0	139350	0.01471
Girardi -0.2	138601	0.00947
Girardi -0.4	137780	0.00605
Girardi -0.6	136913	0.00385
Girardi -0.8	136407	0.00244
Girardi -1.0	135531	0.00155
Girardi -1.2	135167	0.00098
Girardi -1.5	134844	0.00049
Girardi -1.8	134573	0.00025
Girardi -2.1	127889	0.00012

Initial isochrones were created through Hertzsprung-Russell diagrams, where the log of the effective temperature was plotted against the log of the luminosity for every star in each cluster, as shown in Figure 4. This illustrates the diversity of evolution that each cluster had undergone, through the position of their turn-off points, and the extent of their horizontal branches. A composite of all 11 isochrones with a heatmap of their metallicities was plotted to help further express this notion.

H-R diagrams are useful for intragalactic clusters, however, for extragalactic clusters the use of integrated colour over temperature is more appropriate. Therefore, a Colour-Magnitude diagram (CMD), an alternative isochrone method, was chosen, as it utilizes only the magnitude of two wavelengths. Using the filter lengths mentioned previously, each cluster was plotted as six different CMDs, one for every colour ratio that was used. The standard filter ratios were F435W-F555W, F435W-F606W, F475W-F814W, F475W-F850LP, F555W-F814W, and F606W-F814W. Figure 5 shows a sample of the cluster CMDs using the F475W-F814W ratio, along with an additional composite image of the two clusters with the minimum and maximum metallicity value.

The next step was to integrate each cluster down to a singular point, as if to simulate what they would look like if viewed from a long distance. To do this, the magnitudes needed to be converted into luminosities, as magnitude is a unitless metric, while luminosity was measured in watts. The conversion function is represented by Equation 1, where L is the luminosity, M is the magnitude, and k is a conversion constant.

(1)
$$L = 10^{-0.4(M-k)}$$

A constant of 20 was used for k as it gave values that were of a reasonable magnitude to work with. Each star magnitude was converted to luminosity for all six wavelengths. They were then summated and converted back into an integrated magnitude. This was accomplished by using Equation 2.

(2)
$$M = k - 2.5(\log_{10} L)$$

The integrated colour was calculated by subtracting the specific integrated magnitudes denoted by the colour ratios. By plotting the known metallicity values from Table 1 against the integrated colour of the cluster, Colour-Metallicity diagrams (CMetD) were created, as shown in Figure 6. Multi-step linear trendlines were fitted to each CMetD, as shown in Figure 7, with Table 2 indicating the formula associated for each step of each diagram.

To check the viability of these trends, further tests were conducted using real data. A supergiant cD type galaxy called NGC 6166 was utilised for this. Using photometric data obtained from the HST ACS/WFC and WFC3 cameras within the F475W and F814W filters, integrated colours were calculated for the 5557 clusters surrounding the galaxy.[19] With each point already exhibiting integrated properties, a CMetD could be directly created, as is shown in Figure 9. By inverting the formulas found for the F475W-F814W colour ratio of the modelled clusters, it was possible to apply them to the integrated colours of the NGC 6166 clusters and yield their metallicity.

A notable difference in cluster density on either side of the pivot point (as seen in Figure 10), suggested the distribution should be further explored. Figures 11 and 12 show frequency histograms of the integrated colour of the clusters, and the metallicities of the clusters, respectively. The optimal bin width for each was calculated using Scott's normal reference rule, which comes in the form of Equation 3, where σ is the standard deviation and n is the number of data points.[20]

(3)
$$h = \frac{3.49\sigma}{\sqrt[3]{n}}$$

The optimal number of bins was calculated using a function in the form of Equation 4, where k is the number of bins, x is the data set, and h is the bin width.

(4)
$$k = \left\lceil \frac{\max x - \min x}{h} \right\rceil$$

The optimal number of bins for colour was 28, and 30 for metallicity. The non-gaussian distribution they both presented, with their pairs of distinct peaks, suggested the presence of subpopulations. To confirm this, a bimodal gaussian fit was applied to each, using the *curve_fit* routine from the *SciPy* library to optimize them, with the subsequent curves being seen in Figures 13 and 14.

RESULTS

Panels a through k of Figure 4 have plotted the log of the effective temperature against the log of the luminosity for every star in each cluster. Unlike those shown in Figure 2 and 3, each cluster follows only a single isochrone, as all the stars are the same age. As each cluster represents a theoretical model, their stars match the trend that would be given by an idealized isochrone. Each cluster initially follows a main-sequence path (with each sequentially increasing in temperature in a range of 3.35-3.50) until the stars have exceeded 1 $L_\odot$ (solar luminosity). There, each cluster has a sharp turn-off point where the stars begin to cool yet retain their present luminosity, until suddenly their luminosity begins to increase rapidly. This transition occurs when the stars have entered the Red Giant branch, a period when hydrogen fusion in the core has been completed, and fusion from the hydrogen shell surrounding the new helium core causes the star's envelope to expand.[21] This continues until the internal pressure and temperatures of the star grow to where helium fusion is enabled.[22] This can be seen in panels a through k of Figure 4 where the stars begin to increase in temperature again but decrease in luminosity. The clusters with the lowest metallicities (panels i, j, and k of Figure 4) also exhibit the beginnings of the horizontal branch, a stable period where both helium and hydrogen fusion occur. Panel l of Figure 4 is a composite image of all eleven clusters. It also illustrates each cluster's metallicity in a heatmap, with metallicities decreasing as the stars become cooler and redder (to a minimum of log(Z/Z$_{Sun}$) = -2.091), and increasing with the stars becoming hotter and bluer (to a maximum of log(Z/Z$_{Sun}$) = 0.171). The use of log (Z/Z$_{Sun}$) normalized for solar metallicity values, with values of 0 matching that of the Sun.

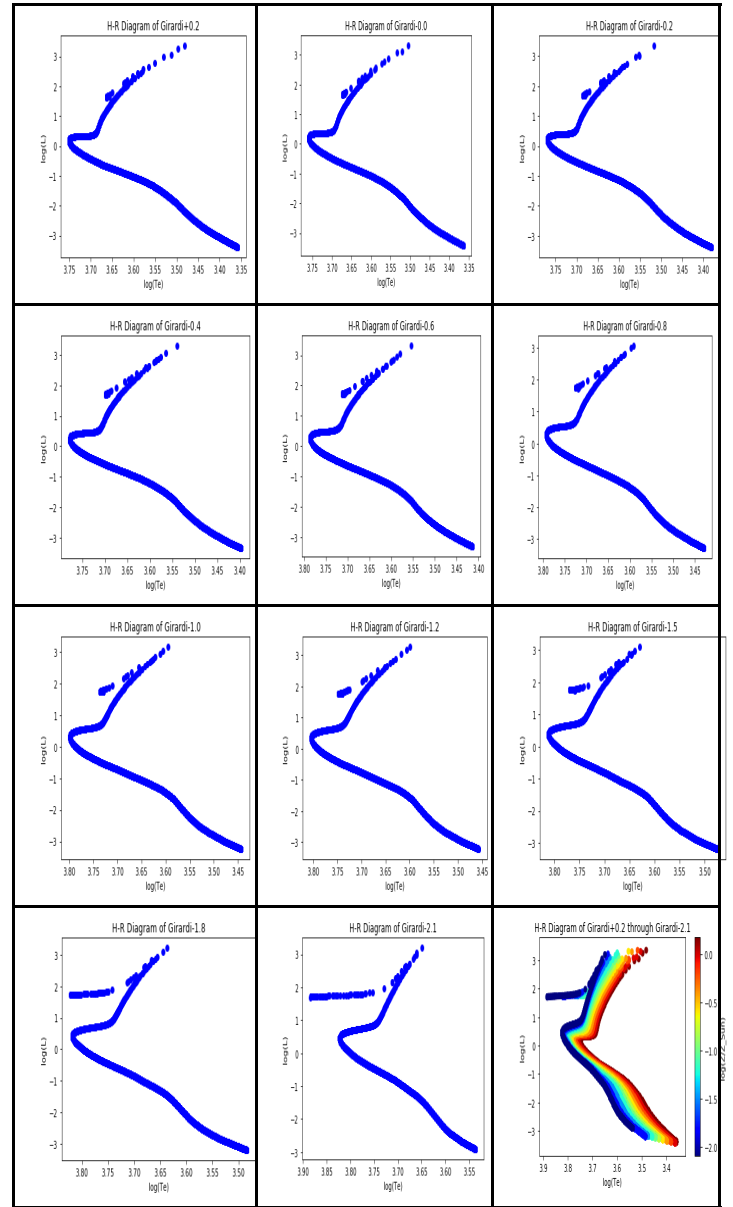**Figure 4.** Panels a − k. Hertzsprung-Russell diagrams of the 11 Girardi clusters and Panel l. Composite image of Panels a − k with a metallicity heatmap in solar units.

Panels a through k of Figure 5 show the CMD isochrones of the same eleven Girardi clusters, with the colour ratio of *F475W-F814W*. They present the same overall structure for each, with the turn-off point, the red giant branch, and the horizontal branch all being visible. Panel l of Figure 5 is a composite image of the two clusters with the maximum and minimum metallicity value, with Girardi -2.1 (Z = 0.00012) being in blue, and Girardi +0.2 (Z = 0.02259) being in red, matching the relation seen in panel l of Figure 4.
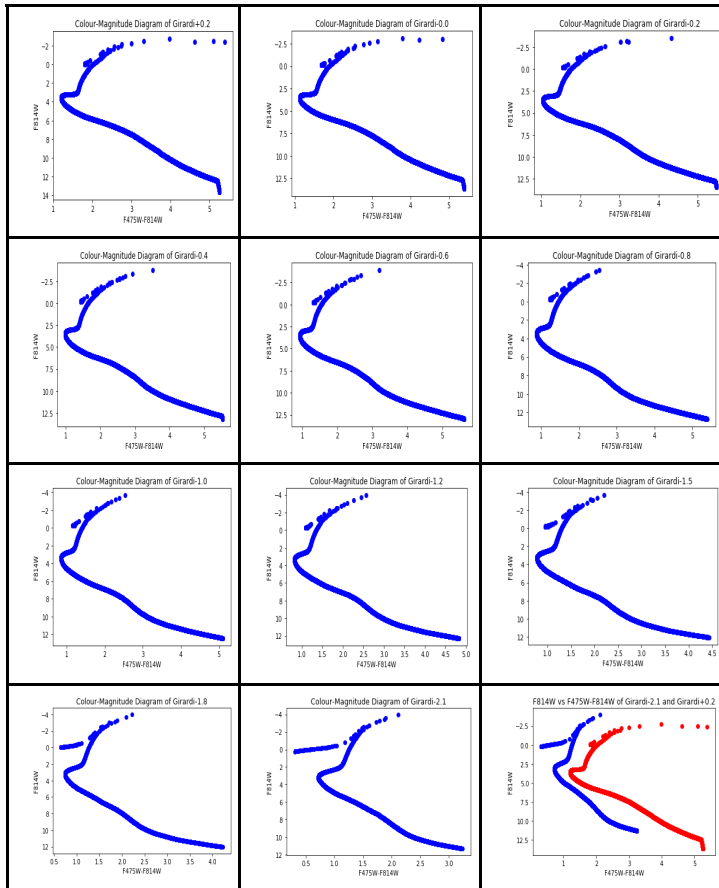
Figure 5. Panels a − k. Colour-Magnitude diagrams of the 11 Girardi clusters. Panel l. Composite image of panels a − k with panel a being coloured red and panel k being coloured blue to represent their relative difference in metallicity.

The panels of Figure 6 depict the CMetDs for all six colour ratios. Each panel has the same positioning on the x-axis as the log of their metallicity remains constant. The range of the integrated colours are only slightly variable, causing a consistent overall relationship between the clusters.
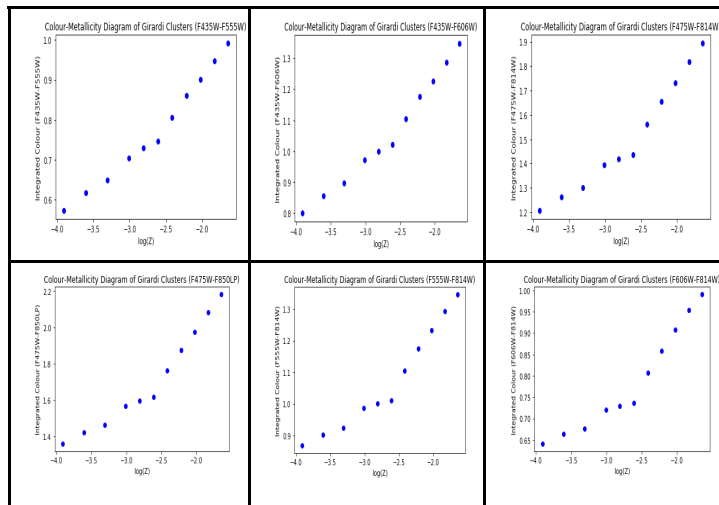
Figure 6. Colour-Metallicity diagrams for the 11 Girardi clusters with colour ratios of F435W-F555W, F435W-F606W, F475W-F814W, F475W-F850LP, F555W-F814W, F606W-F814W, respectively.

The panels of Figure 7 show the panels of Figure 6 with their respective increasing two-step linear trends and equations. Table 2 contains the formulas for the metal-poor trend and the metal-rich trend for each of the diagrams.
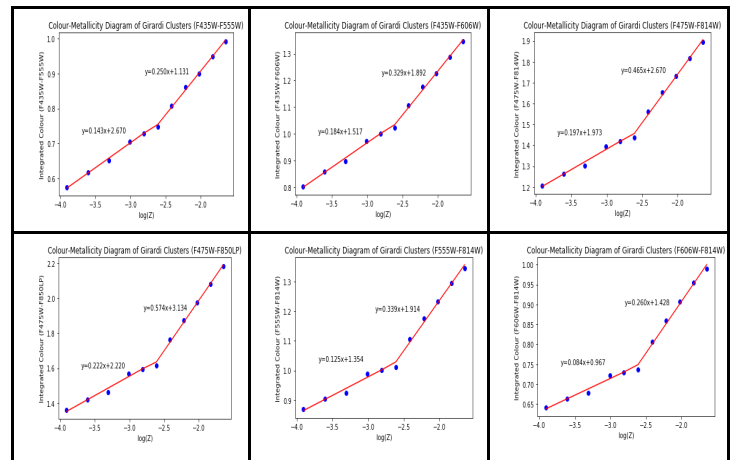

Figure 7. Copies of Figure 6 panels with their respective trendlines and equations for the colour-metallicity relation, for all 11 Girardi clusters, and for each of the six colour ratios.

Table 2. Formulas of the metal-poor and metal-rich trends for each of the colour-metallicity

Colour Ratio	Metal-poor	Metal-rich
F435W-F555W	$y = 0.143x + 2.670$	$y = 0.250x + 1.131$
F435W-F606W	$y = 0.184x + 1.517$	$y = 0.329x + 1.892$
F475W-F814W	$y = 0.197x + 1.973$	$y = 0.465x + 2.670$
F475W-F850LP	$y = 0.222x + 2.220$	$y = 0.574x + 3.134$
F555W-F814W	$y = 0.125x + 1.354$	$y = 0.339x + 1.914$
F606W-F814W	$y = 0.084x + 0.967$	$y = 0.260x + 1.428$

Figure 8 shows the CMD of the NGC 6166 clusters, helping to visualise the decrease in cluster concentration as they increase in brightness. The inversion of the F475W-F814W formulas for the metal-poor portion and the metal-rich portion were found to be $y = 5.076x + 10.015$, and $y = 2.151x + 5.742$, respectively. The manual pivot point was chosen to be F475W-F814W = 1.4607, as that is the intersection point of both functions. Figure 9 shows the CMetD that is created when those equations and pivot point are applied to the clusters of NGC 6166. Figure 10 shows a portion of Figure 9 isolated on the pivot point, showing the change in cluster density between the two segments.
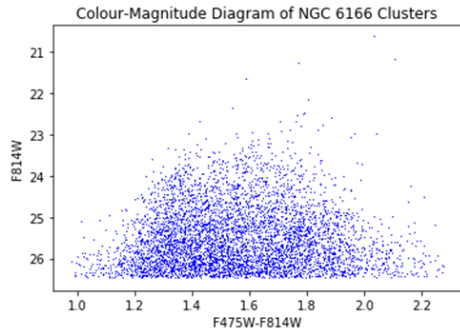
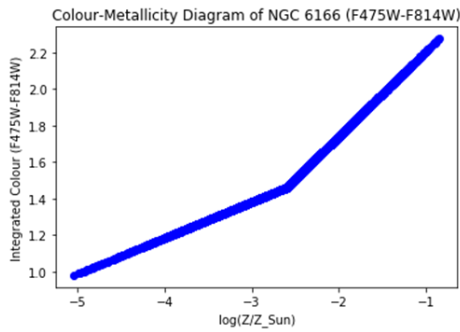**Figure 8.** A colour-magnitude diagram of the clusters of NGC 6166.

Figure 9. A colour-metallicity diagram of the clusters of NGC 6166 using the inverted formula and pivot point of the trendlines from the colour respective Girardi clusters.
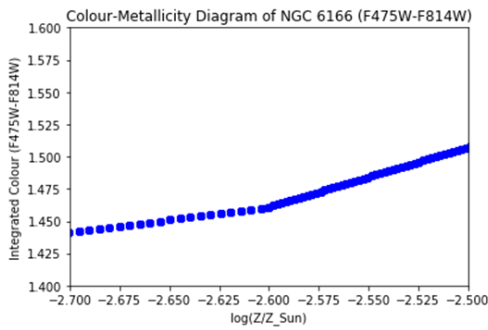

Figure 10. An isolated portion of Figure 9 showing the difference in density between the two metallicity populations.

Figures 11 and 12 show the frequency distribution of the clusters for their colour and metallicity, respectively.
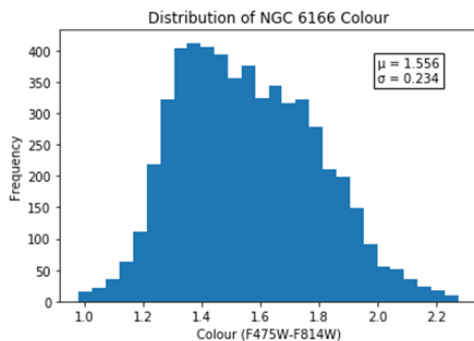

Figure 11. Frequency distribution of the F475W -F814W colour of the NGC 6166 clusters, showing a non-gaussian right-skewed structure.
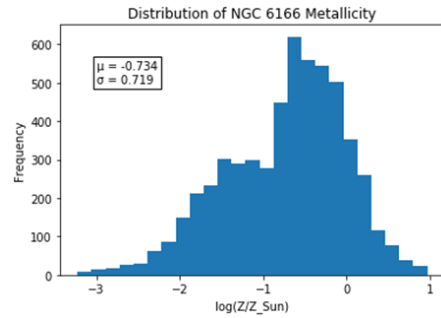

Figure 12. Frequency distribution of the log of the metallicity in solar units of the NGC 6166 clusters, showing a definite non-gaussian left-skewed structure.

Figure 13 shows the fit of the colour distribution, with the metal-poor gaussian curve in blue (with a mean of μ = 1.343), and the metal-rich gaussian curve in red (with a mean of μ = 1.634). The standard deviation of the metal-rich is more than double that of the metal-poor, being σ = 0.220 and σ = 0.101, respectively. Figure 14 shows the fit of the metallicity distribution, again with the metal-poor gaussian curve in blue (μ = -1.587), and the metal-rich gaussian curve in red (μ = -0.734). The standard deviation of the metal-rich is similar to that of the metal-poor, with them being σ = 0.456 and σ = 0.389, respectively.
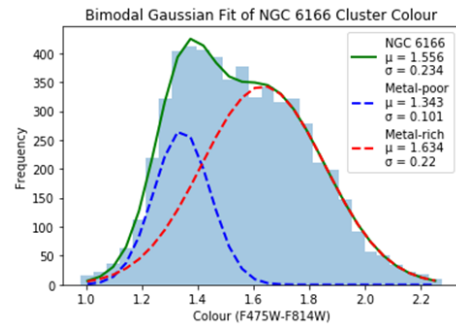

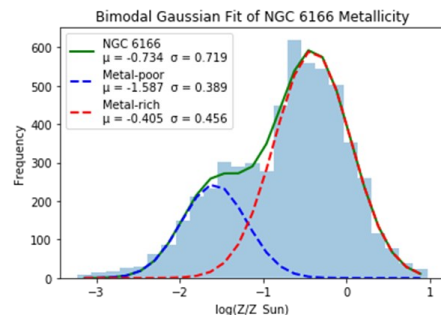**Figure 13.** A bimodal gaussian fit applied to the colour distribution of the NGC 6166 clusters.

Figure 14. A bimodal gaussian fit applied to the metallicity distribution of the NGC 6166 clusters.

DISCUSSION

By looking at each cluster model through Hertzsprung-Russell diagrams (Figure 4), it was possible to validate the idealized nature of their isochrones. By confirming that the clusters followed the idealized trends, it inferred this project might lead to a relationship between colour and heavy element abundance that yield a result closer to the true theoretical relationship. The CMDs of each cluster followed the general structure of their H-R diagrams as each presented clear turn-off points, red giant branches, and horizontal branches in Figure 5. For this reason, it was possible to continue and find the integrated magnitude of each cluster. CMetDs were created using the integrated colour of the six ratios, shown in Figure 6. The consistency of the trends between all of the ratios simplified the process of creating a useful correlation between the cluster's integrated colour and its metallicity. The trend appeared to be an increasing piecewise linear function, which allowed for simpler methods of calculating the correlation (Figure 7). A linear best fit was applied to the segments separated by a manually chosen pivot point. The point, however, was consistent throughout all the CMetDs, being at the same metallicity condition where the Girardi -0.8 cluster sat (Figure 7).

Although Figure 8 shows a vast, chaotic distribution of the NGC 6166 clusters, when the *F475W-F814W* model equations were applied, it forced the clusters to take on the idealized two-step linear structure shown in Figure 9. This is not interesting by itself, but when isolating in on the pivot point, like in Figure 10, a large difference in density can be seen between the two populations. The population in the metal poor region is much less densely populated than those in the metal rich region . Figures 11 and 12 focus on the distribution of the colour and metallicity. Although both figures show a non-gaussian relationship, the metallicity distribution is much more distinct.

A bimodal gaussian fit was successfully applied to both clusters, as Figures 13 and 14 show. The fits found in the metallicity distribution strongly suggest that the clusters of NGC 6166 are divided into at least two subpopulations, with one containing metal-poor clusters, and the other containing metal-rich clusters. The mean metallicity of each cluster (μ = -1.587 and μ = -0.734, respectively) shows that even the majority of the metal-rich clusters have lower metallicities than our Sun, validating the advanced age of both populations. The presence of these distinct cluster populations also indicates the high probability of galactic mergers within the history of NGC. This fits well with the research stating NGC 6166 is a brightest cluster galaxy, having likely evolved from complex mergers during its assembly.[23] The relative number of clusters in the two populations, as well as a larger standard deviation for the metal-rich (σ = 0.456) and smaller deviation for the metal-poor (σ = 0.389), also suggest the

merger of a younger, larger galaxy, with an older, smaller galaxy.

LIMITATIONS

The use of only 11 models to create the integrated colour-metallicity relationship most likely gave an incomplete and simplified version of what the true metallicity function is. The manual placements of pivot points for linear steps was not a sustainable method for calculations, however, it was a necessity for the limited computational skill of the author. Further work should then be completed, with both real and modelled data, in order to create a more realistic function of determining metallicity from integrated colour. The models used in this project increased by $\log(Z)$ = 0.2 - 0.3, and if the missing intermediate models were added it could lead to a more complicated or realistic function. It is possible that this more advanced function might find increased levels of cluster subpopulations, helping to broaden the understanding of certain galactic formations through these fingerprints of evolution.

SUMMARY

This project used 11 computational globular cluster models, with a metallicity range of $\log(Z/Z_{Sun})$ = -2.091 to 0.171, to create six mathematical relationships between the integrated colour of clusters and the metallicity of its stars. This was done through the creation of H-R diagrams and CMDs in order to subsequently convert the data to create integrated colour-metallicity diagrams that covered the colour ratios of F435W-F555W, F435W-F606W, F475W-F814W, F475W-F850LP, F555W-F814W, and F606W-F814W. The viability of the calculated F475W-F814W relationship was confirmed through the use of real colour data from 5557 clusters surrounding the supergiant galaxy NGC 6166, through the creation of a corresponding colour-metallicity diagram. A histogram taken of the cluster metallicity suggested a more complicated distribution than a standard gaussian curve. A *curve_fit* routine was applied and it showed a bimodal gaussian fit of metal-poor and metal-rich subpopulations, suggesting at least one merger within the galaxy's formational past, which is consistent with the literature.

ACKNOWLEDGEMENTS

REFERENCES

(1) Carney BW, Harris WE. Star Clusters: Saas-Fee Advanced Course 28. Lecture Notes 1998 Swiss Society for Astrophysics and Astronomy [Internet]. Labhardt L, Binggeli B, editors. Berlin Heidelberg: Springer-Verlag; 2001 [cited 2021 Feb 5]. (Saas-Fee Advanced Course). Available from: https://www.springer.com/gp/book/9783540676461

(2) Beasley MA. Globular cluster systems and galaxy formation. arXiv:200304093 [astro-ph]. 2020;245−77.

(3) Harris WE. A New Catalog of Globular Clusters in the Milky Way. arXiv:10123224 [astro-ph] [Internet]. 2010 Dec 14 [cited 2021 Feb 1]; Available from: http://arxiv.org/abs/1012.3224

(4) Harris WE, Racine R. Globular clusters in galaxies. Annual Review of Astronomy and Astrophysics. 1979;17:241−74.

(5) Gingerich O. Shapley's Model of the Universe. Astrophysical Journal. 1999;525:135−6.

(6) Hubble, NASA. Caldwell 42 [Internet]. 2011 [cited 2021 Feb 5]. Available from: https://commons.wikimedia.org/wiki/File:Caldwell_42.jpg

(7) Harris WE. Massive star clusters in galaxies. Philosophical Transactions: Mathematical, Physical and Engineering Sciences. 2010;368(1913):889−906.

(8) Richtler T, Larsen S, editors. Globular Clusters - Guides to Galaxies: Proceedings of the Joint ESO-FONDAP Workshop on Globular Clusters held in Concepción, Chile, 6-10 March 2006 [Internet]. Berlin Heidelberg: Springer-Verlag; 2009 [cited 2021 Feb 1]. (ESO Astrophysics Symposia). Available from: https://www.springer.com/gp/book/9783540769606

(9) Sarajedini A, Bedin L, Chaboyer B, Dotter A, Siegel M, Anderson J, et al. The ACS Survey of Galactic Globular Clusters. I. Overview and Clusters Without Previous HST Photometry. AJ. 2007 Apr;133(4):1658−72.

(10) Ramirez I. Theoretical isochrones from the stellar models by Leo Girardi and collaborators (Padova) for near-solar metallicity and a range of ages. [Internet]. 2017 [cited 2021 Apr 4]. Available from: https://commons.wikimedia.org/wiki/File:Isochrones_of_several_ages.png

(11) Jørgensen BR, Lindegren L. Determination of stellar ages from isochrones: Bayesian estimation versus isochrone fitting. Astronomy and Astrophysics. 2005 Jun 1;436:127−43.

(12) Harris WE, Harris GLH, Alessi M. A Catalog of Globular Cluster Systems: What Determines the Size of a Galaxy's Globular Cluster Population? ApJ. 2013 Jul;772(2):82.

(13) Bressan A, Marigo P, Girardi Léo, Salasnich B, Dal Cero C, Rubele S, et al. PARSEC: stellar tracks and isochrones with the PAdova and TRieste Stellar Evolution Code. Monthly Notices of the Royal Astronomical Society. 2012 Nov 1;427:127−45.

(14) Chen Y, Girardi L, Bressan A, Marigo P, Barbieri M, Kong X. Improving PARSEC models for very low mass stars. Monthly Notices of the Royal Astronomical Society. 2014 Nov 1;444(3):2525−43.

(15) Chen Y, Bressan A, Girardi L, Marigo P, Kong X, Lanza A. parsec evolutionary tracks of massive stars up to 350 M☐ at metallicities 0.0001 ≤ Z ≤ 0.04. Monthly Notices of the Royal Astronomical Society. 2015 Sep 1;452(1):1068−80.

(16) Tang J, Bressan A, Rosenfield P, Slemer A, Marigo P, Girardi L, et al. New PARSEC evolutionary tracks of massive stars at low metallicity: testing canonical stellar evolution in nearby star-forming dwarf galaxies. Monthly Notices of the Royal Astronomical Society. 2014 Dec 1;445:4287−305.

(17) Marigo P, Girardi L, Bressan A, Rosenfield P, Aringer B, Chen Y, et al. A New Generation of PARSEC-COLIBRI Stellar Isochrones Including the TP-AGB Phase. The Astrophysical Journal. 2017 Jan 1;835:77.

(18) Pastorelli G, Marigo P, Girardi L, Chen Y, Rubele S, Trabucchi M, et al. Constraining the thermally pulsing asymptotic giant branch phase with resolved stellar populations in the Small Magellanic Cloud. Monthly Notices of the Royal Astronomical Society. 2019 Jun 1;485:5666−92.

(19) Harris WE. Photometric Data for Globular Clusters in BCGs [Internet]. [cited 2021 Apr 5]. Available from: https://www.physics.mcmaster.ca/~harris/BCGdata.html

(20) Scott DW. On optimal and data-based histograms. Biometrika. 1979 Dec 1;66(3):605−10.

(21) Basu S, Hekker S. Unveiling the Structure and Dynamics of Red Giants with Asteroseismology. Front Astron Space Sci. 2020 Aug 4;7:44.

(22) Freedman WL, Madore BF, Hoyt T, Jang IS, Beaton R, Lee MG, et al. Calibration of the Tip of the Red Giant Branch (TRGB). ApJ. 2020 Mar 4;891(1):57.

(23) Harris WE, Blakeslee JP, Whitmore BC, Gnedin OY, Geisler D, Rothberg B. Globular Cluster Systems in Brightest Cluster Galaxies. II: NGC 6166. ApJ. 2016 Jan 20;817(1):58.